PAPER

Check for updates

Dielectric shells as resonant mode tuners: unlocking superior visible-spectrum photon capture in plasmonic perovskite solar cells

Minhaz Mahmood, [a] Mohammad Tariqul Islam,*[ab] Mohamad A. Alawad,[c] Puvaneswaran Chelvanathan,[de] Abdulmajeed M. Alenezi,[f] Mohamed Ouda*[g] and Md. Shabiul Islam*[hi]

A critical barrier to commercializing perovskite solar cells (PSCs) is the trade-off between the efficiency of thick absorbers and the stability of thin films. Advanced light management is essential to resolve this, yet the optimal nanophotonic strategy remains debated. Here, we resolve this debate by systematically comparing planar, dielectric, bare plasmonic, and core–shell architectures within a unified multi-physics framework. We find the core–shell plasmonic design is clearly superior, with the champion CoreAu architecture achieving 21.61% efficiency, a 43% relative enhancement over the 15.11% planar baseline, driven by a J_{sc} increase from 18.22 to 26.34 mA cm^{-2}. The core physical insight is that the dielectric shell acts as an active resonant tuner, enabling the excitation of powerful, higher-order plasmonic modes inaccessible to bare nanoparticles. This unique capability facilitates a strategic shift from specialist near-infrared light trapping to a more effective broadband anti-reflection in the visible spectrum, where solar flux is highest. This work establishes a new design principle for plasmonic PSCs: the shell must be co-optimized as an active optical element to prioritize visible-spectrum photon capture, providing a clear pathway toward ultra-high-efficiency, stable thin-film photovoltaics.

1. Introduction

Metal-halide perovskites have emerged as a transformative class of semiconductor materials, catalyzing unprecedented progress in the field of photovoltaics. Their exceptional optoelectronic properties, including high absorption coefficients, long charge-carrier diffusion lengths, and remarkable defect tolerance, have enabled a meteoric rise in power conversion efficiencies (PCEs) for single-junction devices to over 26%, rivalling established thin-film and crystalline silicon technologies.[1,2] This performance, coupled with the potential for low-cost, solution-based fabrication, positions perovskite solar cells (PSCs) as a leading candidate for next-generation solar energy, with profound implications for terawatt-scale power generation and high-efficiency tandem configurations.[3]

Despite this progress, widespread commercialization remains reliant upon overcoming the challenge of long-term operational stability.[4] A promising strategy to mitigate the intrinsic degradation pathways of perovskite materials involves reducing the absorber layer thickness.[5] Thinner active layers can suppress deleterious ion migration and improve charge extraction, but this introduces a fundamental optical trade-off. As the absorber thickness falls below the optical absorption length, a significant fraction of incident photons, particularly those with near-bandgap energies, are incompletely absorbed.[6] This leads to substantial transmission losses and a corresponding decrease in the short-circuit current density (J_{sc}), creating a critical dilemma where improvements in stability come at the direct expense of PCE. To decouple these competing factors, the implementation of advanced light management is not merely beneficial but essential for realizing the full potential of stable, efficient, thin-film PSCs.

[a] Department of Electrical, Electronic and Systems Engineering, Faculty of Engineering and Built Environment, Universiti Kebangsaan Malaysia, Bangi 43600, Selangor, Malaysia. E-mail: tariqul@ukm.edu.my

[b] Computer and Information Sciences Research Center (CISRC), Imam Mohammad Ibn Saud Islamic University (IMSIU), Riyadh, Saudi Arabia

[c] Department of Electrical Engineering, College of Engineering, Imam Mohammad Ibn Saud Islamic University (IMSIU), Riyadh, Saudi Arabia

[d] Solar Energy Research Institute (SERI), Universiti Kebangsaan Malaysia, Bangi, 43600, Selangor, Malaysia

[e] Pusat Pengurusan Makmal Alami & Fizikal UKM (ALAF-UKM), Universiti Kebangsaan Malaysia, Bangi, 43600, Selangor, Malaysia

[f] Department of Electrical Engineering, Faculty of Engineering, Islamic University of Madinah, Madinah 41411, Saudi Arabia

[g] Department of Telecommunication and Network Engineering, College of Engineering and Technology, University of Doha for Science and Technology, Qatar. E-mail: mohamed.ouda@udst.edu.qa

[h] Centre for Advanced Devices and Systems, Centre of Excellence for Robotics and Sensing Technologies, Multimedia University, Persiaran Multimedia, 63100 Cyberjaya, Selangor, Malaysia. E-mail: shabiul.islam@mmu.edu.my

[i] Faculty of Artificial Intelligence and Engineering, Multimedia University, Persiaran Multimedia, 63100 Cyberjaya, Selangor, Malaysia

This journal is © The Royal Society of Chemistry 2026

J. Mater. Chem. A, 2026, **14**, 14637–14649 | **14637**

Nanophotonics provides a powerful toolkit to overcome this limitation, with two principal strategies dominating the field: plasmonic and high-index dielectric scattering. Plasmonic light trapping utilizes localized surface plasmon resonances (LSPRs) in metallic nanoparticles (*e.g.*, Au, Ag) to generate intense, sub-wavelength electromagnetic near-fields that enhance local absorption.[7] However, this approach is encumbered by two intrinsic loss mechanisms: parasitic (Ohmic) absorption in the metal, which generates heat instead of charge carriers, and non-radiative recombination at the metal–semiconductor interface, which can quench photogenerated carriers.[8] In contrast, the all-dielectric approach employs high-refractive-index nano-structures (*e.g.*, Si, GaInP) that support strong, virtually lossless Mie scattering resonances.[9] These can be engineered to increase the effective optical path length without introducing parasitic absorption or electronic quenching, though the magnitude of near-field enhancement is generally weaker than their plasmonic counterparts.

The parallel existence of these options creates a critical knowledge gap and a strategic bottleneck in the rational design of light-trapping architectures. A third, hybrid approach—the core–shell plasmonic nanostructure—has been proposed as a solution. Numerous experimental studies have successfully demonstrated that embedding core–shell nanoparticles (*e.g.*, Au@SiO$_2$) can enhance PSC efficiency, with reported PCE enhancements of up to 27%.[10] These gains are typically attributed to a combination of electronic passivation by the shell and plasmon-enhanced NIR absorption from the core.[11,12] However, these experimental works present a complex interplay of coupled optical and electronic effects that are difficult to deconstruct, and they have not systematically compared the efficacy of this approach against other nanophotonic strategies.[13] Furthermore, this view largely overlooks the active and potentially decisive optical role of the shell itself.[14] This gives rise to a more fundamental design question: what is the optimal strategy for enhancing a thin-film PSC? Is it more effective to use resonant light trapping to boost absorption where it is weakest (the near-infrared), or to engineer broadband anti-reflection to maximize photon incoupling where the solar flux is highest (the visible spectrum)? To date, a systematic investigation that deconstructs these competing strategies within a single, high-performance device platform is conspicuously absent. To address this gap, we present a comprehensive computational study that systematically compares planar, dielectric, bare plasmonic, and core–shell plasmonic architectures. Our results reveal that the core–shell design's superiority stems not from passive shielding, but from the shell's function as an active resonant tuner. This enables a powerful broadband visible anti-reflection strategy that is inaccessible to other designs, establishing a clear design principle that decisively outperforms the specialized near-infrared light-trapping approaches commonly pursued in the literature.

2. Computational methods

2.1. Coupled optoelectronic framework

The optical and electrical performance of the perovskite solar cell (PSC) architectures was simulated using a comprehensive, multi-

physics computational framework. The methodology involved a two-step process. The optical properties were determined using a commercial-grade finite-difference time-domain (FDTD) solver (Ansys Lumerical FDTD) to calculate the three-dimensional, spectrally-resolved optical generation rate, $G(x,y,z,\lambda)$.[15,16] This generation rate profile subsequently served as the input for the electrical device modeling, which was performed using a finite-element charge transport solver. All simulations were conducted assuming a standard device operating temperature of 300 K.

2.2. Device architecture and optical modeling

The baseline device architecture, depicted schematically in Fig. 1a, consists of a planar multi-layer stack representative of a high-performance inverted p-i-n PSC. The complete layer stack, including material specifications and thicknesses, is detailed in Table S1. The optical constants for all materials were defined using experimentally measured, wavelength-dependent complex refractive index (n, k) data obtained from established literature sources.[17–20] Fig. 1b details the photonic crystal-embedded structure.

For the nanophotonically-enhanced designs, a periodic square array of nanoparticles was embedded at the rear interface of the perovskite absorber layer. A comprehensive para-metric optimization was performed for each material (Ag, Au, GaInP) and geometry (bare sphere, core–shell) to maximize the integrated short-circuit current density. The final optimized geometric parameters for each of the six photonic crystal configurations are summarized in Table S2. The naming convention used throughout this manuscript is as follows: Bare (planar reference), PCAg, PCAu, PCGaInP (bare nanoparticle arrays), and CoreAg, CoreAu, CoreGaInP (core–shell nano-particle arrays). The simulated nanoparticles are idealized as perfectly spherical and uniform to establish the theoretical optimum for each design.
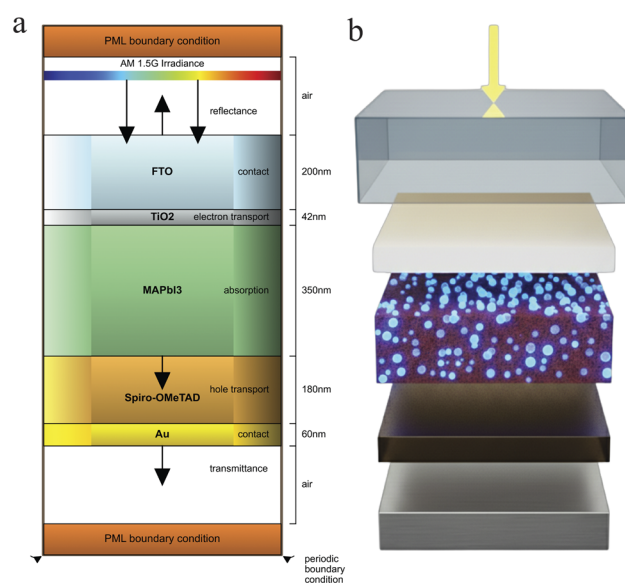

Fig. 1 (a) FDTD simulation structure and (b) photonic crystal-embedded perovskite solar cell structure.

14638 | *J. Mater. Chem. A*, 2026, **14**, 14637–14649

This journal is © The Royal Society of Chemistry 2026

The 3D FDTD simulation domain in Fig. 1a was defined with periodic boundary conditions on the lateral (x and z) axes to model an infinitely repeating array and "steep angle" profile perfectly matched layer (PML) absorbing boundaries with 8 layers on the vertical (y) axis. A broadband plane wave source (300 nm to 900 nm) was used to model normally incident solar illumination under the AM1.5 G spectrum. To simulate unpolarized sunlight, the final results were calculated as the incoherent average of two separate simulations with orthogonal polarizations. A non-uniform conformal mesh was employed with a global mesh accuracy setting of 4, with targeted mesh refinement regions enforcing a maximum mesh step of 5 nm at the critical front interfaces and 2 nm in the immediate vicinity of the nanoparticles to accurately resolve plasmonic near-fields.[21] The simulation was terminated only after the total electromagnetic energy decayed to 10^{-6} of its initial maxima, ensuring full convergence of all resonant phenomena. Moreover, the high precision of the reported performance metrics of this work is a direct result of the deterministic nature of the coupled opto-electronic model and rigorous convergence testing of the FDTD simulations. This ensures that the numerical uncertainty reported in our final device metrics is well below 0.01%.

2.3. Calculation of optical metrics

The spectrally-resolved power absorption density, $P_{abs}(x,y,z,\lambda)$, was calculated from the simulated electric fields within the perovskite layer. For the purposes of this primarily optical study, a key assumption is made: the internal quantum efficiency (IQE) is taken to be 100%.[22,23] This assumes that every photon absorbed within the perovskite active layer generates an electron–hole pair that is successfully collected. The external quantum efficiency (EQE) is considered to be equal to the spectrally-resolved absorptivity of the active layer. The total absorptivity of the active layer, $A(\lambda)$, is calculated from the simulated reflectance $R(\lambda)$ and transmittance $T(\lambda)$ of the full device stack as:

$$A(\lambda) = 1 - R(\lambda) - T(\lambda)$$

The optically-limited short-circuit current density, J_{sc}, which represents the theoretical maximum current assuming perfect charge collection, was then calculated by integrating the product of the EQE and the standard AM1.5 G solar photon flux, $\Phi_{AM1.5\ G}(\lambda)$, over the relevant wavelength range:

$$J_{sc} = q \int_{\lambda_{min}}^{\lambda_{max}} \text{EQE}(\lambda) \cdot \Phi_{AM1.5\ G}(\lambda) d$$

where q is the elementary charge.

2.4. Electrical device modeling

The electrical performance of the devices was subsequently modeled using a drift-diffusion solver.[24,25] The crucial link between the optical and electrical models was the optical generation rate. The spectrally-integrated, three-dimensional

optical generation rate matrix, $G(x,y,z)$, calculated by the FDTD solver for the entire active layer volume, was saved and then directly imported as the generation source term for the electrical simulation. The simulation then solved the Poisson and drift-diffusion equations self-consistently to determine the final device characteristics. The simulation incorporated a comprehensive set of recombination models to ensure a physically realistic description of carrier dynamics. The models included: Shockley-Read-Hall (SRH) recombination, which accounts for non-radiative losses via defect trap states, the dominant loss pathway in most perovskite devices; Radiative (direct) recombination, which represents the fundamental recombination pathway in direct-bandgap semiconductors and sets the thermodynamic limit for V_{oc}; and Auger recombination, a non-radiative process that becomes significant at the high carrier densities present under illumination. The inclusion of these three models provides a robust framework for accurately simulating the performance of high-efficiency PSCs. The key material and device parameters used in the electrical simulation are summarized in Table S3. From the simulated current density–voltage (J–V) curves, the terminal characteristics, including the final self-consistent J_{sc}, V_{oc}, fill factor (FF), and PCE, were extracted. A detailed breakdown of voltage losses was also performed based on the principle of detailed balance, separating the total voltage deficit, (Eg/q) − V_{oc}, into three components: $\Delta V1$ (thermalization loss), $\Delta V2$ (radiative recombination loss), and $\Delta V3$ (non-radiative recombination loss). To isolate the impact of the optical design, the parameters governing $\Delta V3$ were held constant across all simulated devices, thereby creating an idealized electronic platform to rigorously compare the distinct optical strategies.

3. Results and discussion

The performance of a photovoltaic device is fundamentally governed by its interaction with the incident solar spectrum. An effective design must first minimize optical losses $i.e.$ reflection and transmission, to ensure the maximum possible number of photons enters the active material. It must then maximize the absorption of those photons to generate charge carriers. This section presents a systematic analysis that flows from these fundamental optical principles to the final device characteristics, deconstructing the precise mechanisms and strategic trade-offs inherent to each nanophotonic design.

3.1. Nanophotonic control of optical properties: reflection and transmission

The initial interaction of sunlight with the solar cell dictates the upper limit of its performance. The primary optical loss channels, front-surface reflection and parasitic transmission, represent photons rejected without any opportunity for conversion. The integration of nanophotonic structures is intended to mitigate these losses by engineering the device's optical response. A detailed deconstruction of the reflectance and transmittance for each architecture reveals a complex

This journal is © The Royal Society of Chemistry 2026

J. Mater. Chem. A, 2026, **14**, 14637–14649 | **14639**

interplay of resonant coupling and interference, exposing the distinct strategies and trade-offs inherent to each design.

The initial primary optical loss channels are the front-surface reflection and parasitic transmission, which represent photons rejected without absorption. The integration of nanophotonic structures is intended to mitigate these losses by engineering the device's optical response. A detailed deconstruction of the reflectance and transmittance for each architecture reveals a complex interplay of resonant coupling and interference, exposing the distinct strategies and trade-offs inherent to each design.

The device reflectance spectra, presented in Fig. 2b, immediately reveal that the nanophotonic structures induce highly wavelength-selective behaviours. The planar Bare cell establishes the baseline, exhibiting a pronounced reflection peak approaching 0.8 near 710 nm. This is a strong Fabry-Pérot resonance characteristic of the optical cavity formed by the thin-film stack, representing a major loss channel for near-band-edge photons.[26] The devices incorporating dielectric GaInP nanoparticles (PCGaInP and CoreGaInP) not only fail to mitigate this reflection but dramatically worsen it. Both exhibit a sharpened reflection peak near 690 nm, confirming they are detrimental to light incoupling. This resonant lineshape is the classic signature of a Fano resonance, a phenomenon that arises from the interference between a discrete, resonant pathway and a broad, continuum-like pathway. In this context, the broad continuum is the reflection from the planar thin-film stack, while the discrete resonance is a sharp Mie scattering mode supported by the high-index GaInP nanoparticle.[27] At the resonant wavelength, these two pathways interfere destructively in the forward direction, which suppresses transmission into the active layer and leads to a sharp increase in total reflection. This effectively transforms the nanoparticle from a potential light-coupler into a highly efficient, wavelength-selective mirror that actively rejects photons, fully explaining the subsequent collapse in absorption and quantum efficiency for these devices.

Markedly different, the plasmonic devices present two distinct and far more effective strategies. The first, represented by the bare plasmonic particles PCAg and PCAu, is specialized NIR anti-reflection. Both leverage their primary LSPR to create a deep resonant dip in reflectance centered around 740 nm, suppressing reflection from over 0.7 to below 0.1.[28,29] This is a classic light-trapping approach, specifically engineered to efficiently couple weakly absorbed, near-band-edge photons that are lost to reflection in the Bare cell.

The champion CoreAu device executes a completely different and more sophisticated strategy. It achieves excellent anti-reflection in the photon-rich visible spectrum, with a sharp dip near 630 nm. However, this benefit is achieved by introducing two extremely intense reflection peaks at 690 nm and 725 nm, where reflectance again approaches 0.8. This is a critical insight: the CoreAu architecture is not a simple anti-reflector but a complex resonant system that strategically sacrifices performance in narrow spectral bands to maximize photon incoupling across the broader, more intense visible region. This strategic trade-off is quantitatively validated by analyzing each device's photocurrent budget relative to the Bare cell, with the full results presented in Table S4 of the SI. By integrating the photocurrent difference across the solar spectrum, we can separate the total current gained from regions of reduced reflection (J_{gain}) from the current lost in regions of increased reflection (J_{loss}). For the champion CoreAu device, the superior anti-reflection in the visible spectrum yields a massive J_{gain} of 6.79 mA cm^{-2}, while the narrow reflection peaks in the near-infrared correspond to a minimal J_{loss} of only -0.11 mA cm^{-2}. This results in a substantial net gain of 6.68 mA cm^{-2} from reflection management alone, providing clear quantitative evidence that this strategy is highly effective. The CoreAg device displays a hybrid behavior, with a reflection peak near 730 nm followed by a broader region of suppressed reflection, positioning its strategy between that of the bare plasmonics and CoreAu.

The transmittance spectra in Fig. 2a quantify photon leakage through the rear of the device. For wavelengths beyond the perovskite bandgap ($\sim$780 nm), the Bare and CoreGaInP devices exhibit the highest transmittance, confirming significant
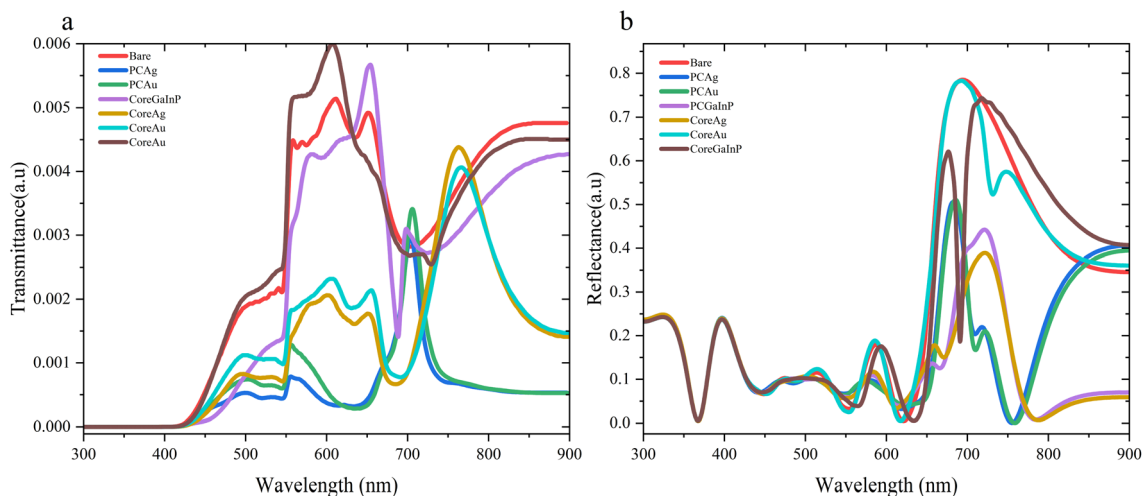

Fig. 2 (a)Transmittance and (b) reflectance spectra.

photon loss. The plasmonic designs, by virtue of the opaque metal nanoparticles, function as near-perfect back-reflectors and completely eliminate this transmission loss channel.[30,31] This dual functionality, simultaneously manipulating front-surface reflection while guaranteeing zero rear-surface transmission, is a fundamental advantage of the plasmonic approach that underpins its potential for dramatic performance enhancement.

3.2. Active absorption and spectral responsivity

The absorption analysis is best understood by dividing the spectrum into two critical regions: the visible absorption band (400–650 nm), where the perovskite is a strong absorber and solar flux is highest, and the near-infrared (NIR) light-trapping region ($\lambda > 650$ nm), where the perovskite is intrinsically weak.[31]

Fig. 3a presents the active absorption in the perovskite layer, while Fig. 4 shows the corresponding spectral responsivity (SR), which directly translates this absorption into potential photocurrent. In the crucial NIR region, the Bare cell and the dielectric PCGaInP and CoreGaInP devices perform poorly, with their absorption and responsivity falling precipitously towards the band edge. This confirms the failure of the dielectric Fano resonance to enhance optical path length for weakly absorbed photons.

The plasmonic devices, however, reveal two differing and successful strategies. The first is specialized NIR light trapping, executed effectively by PCAg, PCAu, and CoreAg. These architectures exhibit a powerful and broad resonant absorption peak centered near 780 nm, boosting the SR to exceptional values greater than 0.5 A W^{-1}. This feature is the classic signature of a highly effective light-trapping mechanism, likely a plasmonically-coupled waveguide mode, specifically engineered to harvest near-band-edge photons that would otherwise be lost.[32]

The champion CoreAu device employs a completely different approach. In the NIR, it exhibits a profound absorption minimum, a resonant "dead zone" between 670 nm and 750 nm where its performance is the worst of all plasmonic configuration. This null absorption directly corresponds to the intense
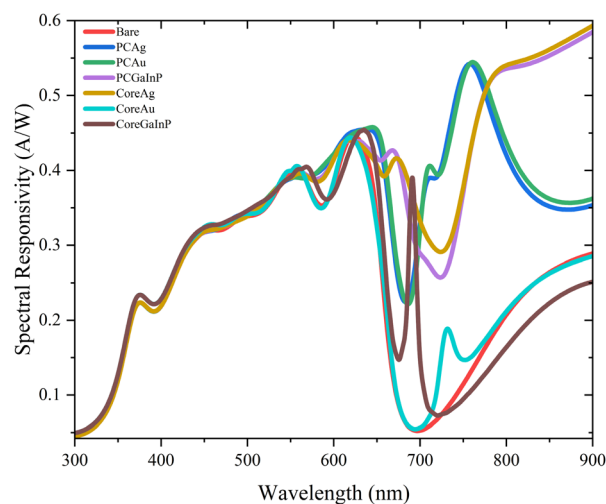

Fig. 4 Spectral Responsivity (SR).

reflection peaks identified previously, confirming that this specific resonance strongly rejects light rather than coupling it. The key to the CoreAu device's success therefore lies in the main visible absorption band. Here, where the primary role of nanophotonics shifts from light trapping to improving incoupling *via* anti-reflection, the CoreAu device is the top performer. Across this entire window, its absorption and SR are consistently among the highest, capitalizing on its unique resonant structure to maximize photon capture in the most intense part of the solar spectrum.

This analysis reveals two distinct design philosophies: PCAg, PCAu, and CoreAg are optimized as specialist NIR light trappers, excelling at capturing low-energy photons. In contrast, CoreAu is optimized as a superior broadband visible anti-reflector, sacrificing all performance in the NIR to achieve unparalleled photon incoupling in the 400–650 nm range.

For the NIR-specialist devices, parasitic losses in Fig. 3b, are correlated with their regions of enhanced active absorption, representing the classic trade-off where strong plasmonic
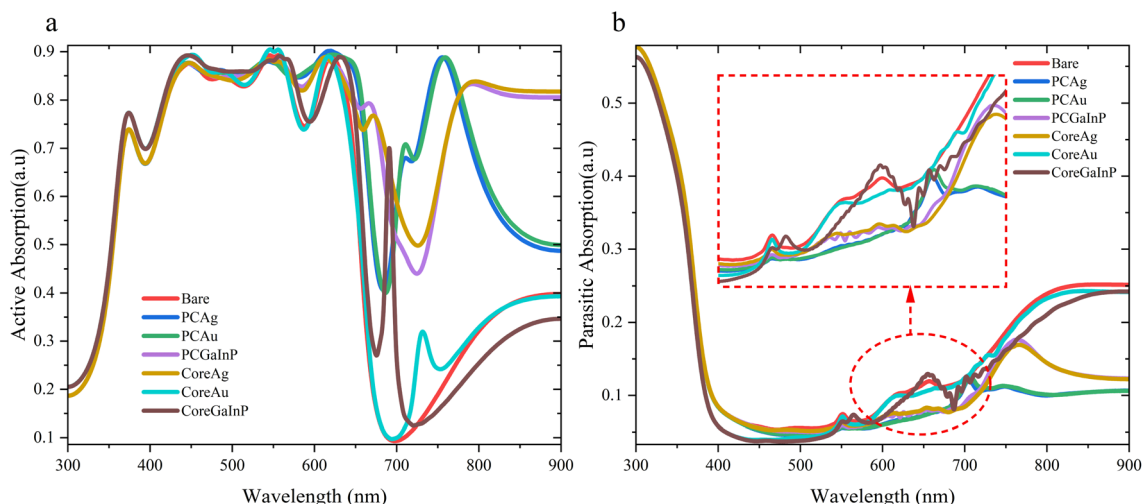

Fig. 3 (a) Active absorption spectra and (b) parasitic absorption spectra.

enhancement is accompanied by some ohmic loss.[33] Conversely, the parasitic peak for the CoreAu device aligns with its NIR "dead zone," suggesting its resonance is not only highly reflective but also dissipative. The ultimate device efficiency will depend on the integrated effect of these competing strategies. The success of the CoreAu architecture implies that for this thin-film perovskite system, maximizing photon capture in the high-flux visible band provides a greater net benefit to J_{sc} than specializing in capturing the fewer available photons near the band edge.[34]

3.3. Benchmarking performance against thermodynamic limits

To quantitatively assess the efficacy of each nanophotonic strategy, we benchmark their total absorption ($A = 1 - R - T$) against fundamental physical limits, as shown in Fig. 5. The performance of each device is compared against two key metrics: the Single-Pass Limit (Beer–Lambert absorption for a 350 nm film) and the Yablonovitch Limit, the thermodynamic maximum for a perfect Lambertian light-trapper.[35,36] The Yablonovitch limit, A_{yab} is given by:[35]

$$A_{yab}(\lambda) = \frac{\alpha(\lambda)}{\alpha(\lambda) + \dfrac{1}{4n(\lambda)^2 d}}$$

where $\alpha(\lambda)$ is the material's absorption coefficient, $n(\lambda)$ is its refractive index, and d is the film thickness. This framework provides a rigorous evaluation of each design's ability to enhance the effective optical path length.

The plot provides definitive evidence for the failure of the dielectric nanophotonic strategy in this architecture. The PCGaInP and CoreGaInP devices exhibit a sharp dip in absorption centered at 690 nm, where their performance plummets far below even the single-pass limit. This occurs because the single-pass limit assumes perfect incoupling of light ($R = 0$), whereas these devices are intensely reflective at this wavelength due to the Fano resonance. Their performance is therefore significantly worse than the Bare cell, which itself

closely tracks the single-pass limit, confirming its status as a poor light-trapper.

In contrast, the NIR-specialist devices, PCAg, PCAu, and CoreAg, demonstrate exceptional light-trapping performance where it is most needed. For wavelengths greater than 700 nm, their absorption curves are dramatically elevated above the single-pass limit and closely approach the thermodynamic Yablonovitch limit. The resonant absorption peak near 780 nm for the PCAg and PCAu devices nearly touches this limit, signifying an almost physically perfect light-trapping efficiency that maximizes the optical path length to its theoretical potential. This quantitatively confirms their status as elite NIR light-trappers.

The CoreAu device presents a completely different and more complex strategic trade-off. In the NIR region ($\lambda > 700$ nm), it is a demonstrably poor light-trapper; its absorption curve shows a deep null around 725 nm, falling below the single-pass limit due to high reflection. However, its strength lies in the main visible absorption band (600–650 nm), as shown in the inset. In this photon-rich region, where the perovskite is already a strong absorber, the CoreAu curve consistently follows the Yablonovitch limit more closely than any other design. While the absolute gains in path length are smaller here, this indicates superior light incoupling and anti-reflection performance. This plot, therefore, quantitatively deconstructs the two competing successful strategies: PCAg, PCAu, and CoreAg achieve near-perfect light trapping in the NIR, while the CoreAu device sacrifices NIR performance to achieve superior light coupling in the visible spectrum.

3.4. Diagnosing internal losses and light coupling with quantum efficiency analysis

The External Quantum Efficiency (Fig. 6a) represents the probability that an incident photon generates a collected electron, thus encompassing all optical losses. The Internal Quantum Efficiency (Fig. 6b) is the probability that an absorbed photon generates a collected electron, providing a direct measure of internal loss mechanisms like parasitic absorption.[37] The relationship is given by:

$$IQE(\lambda) = \frac{EQE(\lambda)}{1 - R(\lambda) - T(\lambda)} = \frac{\text{Active absorption}}{\text{Total absorption}}$$

The EQE spectra directly quantify the outcomes of the two strategic approaches identified previously, with the NIR-specialist devices (PCAg, PCAu, CoreAg) showing a strong peak near 780 nm, and the champion CoreAu excelling in the 580–650 nm visible window, with a dip at around 720 nm, and another sustained peak from 760 nm and beyond.

The IQE spectra provide the critical diagnostic insight into internal loss pathways. The non-plasmonic devices (Bare, PCGaInP, CoreGaInP) act as a crucial control group, all exhibiting a consistently high and flat IQE approaching 0.95. This demonstrates that the pristine perovskite active layer is highly efficient at converting absorbed photons into charge carriers,
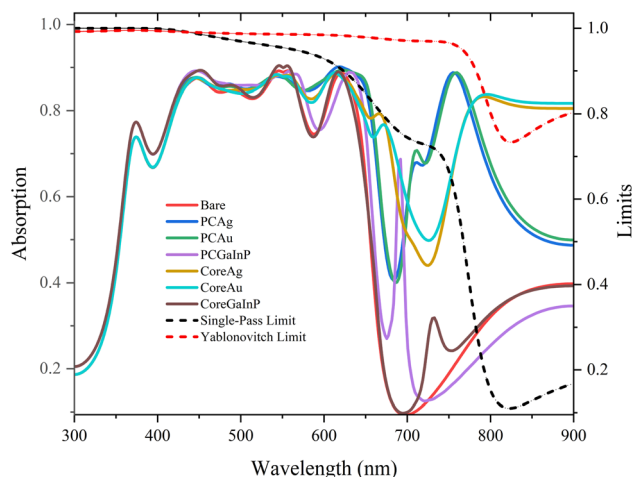

Fig. 5 Light trapping analysis vs. theoretical limits.

14642 | J. Mater. Chem. A, 2026, 14, 14637–14649

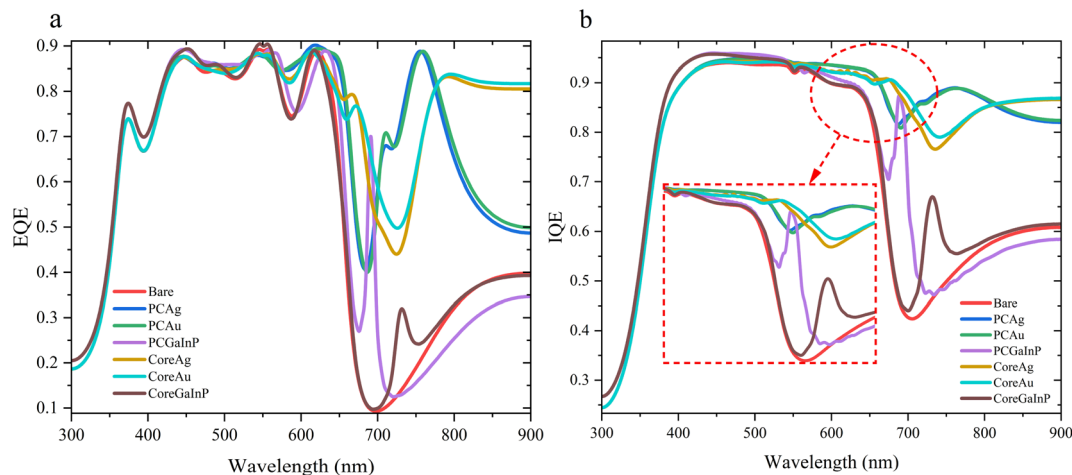This journal is © The Royal Society of Chemistry 2026

Fig. 6   Quantum efficiencies: (a) EQE and (b) IQE.

and that the poor EQE of these devices is almost exclusively due to external optical losses such as high reflection.

The introduction of plasmonic nanoparticles fundamentally alters this internal efficiency. While all four plasmonic devices maintain a high IQE in the non-resonant region ($\lambda < 650$ nm), they each exhibit a sharp, pronounced dip in the 670–780 nm range. This is the unambiguous signature of parasitic absorption (Ohmic loss) in the metal nanoparticles, where a significant fraction of absorbed photons generates heat instead of electron–hole pairs.[38] The specific features of these IQE dips reveal the extent of this intrinsic trade-off. The CoreAu device exhibits an exceptionally deep and sharp IQE dip that plummets below 0.4 at 725 nm, aligning perfectly with its reflective "dead zone." This confirms that the small fraction of light that is not re-flected at this resonance is predominantly dissipated as heat. The NIR-specialist devices also pay a price for their enhance-ment, with significant IQE dips centered around 710 nm.

Further analysis, detailed in the SI, provides a complete picture of the optical trade-offs. The IQE/EQE ratio (see Fig. S2), a proxy for light incoupling, confirms that from a purely optical perspective, bare plasmonic particles offer the most potent peak anti-reflection. However, this metric is inadequate, as it neglects the well-established electronic consequences of placing a bare metal nanoparticle in direct contact with the perovskite, which is known to introduce severe non-radiative recombination centers and possible short-circuit pathway.[39] Thus, the core–shell architecture is the necessary solution.[40] Our study, there-fore serves to isolate and quantify the optical price of this solution, revealing that a minor sacrifice in peak optical coupling is the required trade-off for an electronically viable device.[41] The effective optical density of each architecture is quantified by the effective absorption coefficient and skin depth (see Fig. S3).[42] This confirms that the NIR-specialist devices dramatically reduce the skin depth at longer wavelengths, while the champion CoreAu device achieves the lowest skin depth in the visible spectrum, proving it makes the device more optically dense and absorptive in the most photon-rich part of the solar spectrum.

3.5.   Visualizing resonant modes and light trapping mechanisms

The spectral data provides a quantitative account of what optical enhancements occur; we now turn to a spatial analysis to understand how and where they are physically realized. Fig. 7 presents the spectrally-resolved optical generation rate within a cross-section of the perovskite active layer for each architec-ture. To best visualize the distinct spatial features of the reso-nant modes, the colour scale for each panel is normalized to its own maximum value, which is indicated within the plot. This direct visualization of the underlying physics provides a clear foundation for understanding the vast differences in device performance.

The planar Bare cell (Fig. 7A) serves as the essential baseline, revealing a clear, periodic pattern of alternating horizontal bands, the definitive signature of a one-dimensional standing wave pattern caused by thin-film interference.[43] This establishes that even the planar cell possesses a rudimentary light management mechanism. The goal of advanced nanophotonics is to surpass this weak 1D effect with a more powerful, three-dimensional light concentration strategy. The integration of the dielectric PCGaInP nanoparticle (Fig. 7B) fails to provide any meaningful enhancement. Instead of concentrating light, the nanoparticle creates a distinct "shadow" region beneath it where the generation rate is suppressed. This visual evidence provides the direct physical explanation for the catastrophic dip in its spectral performance, confirming that the Fano-like resonance actively rejects light from the active layer.

The introduction of bare plasmonic nanoparticles completely transforms the physics of light absorption. Both the PCAg (Fig. 7C) and PCAu (Fig. 7E) nanoparticles generate an intense, highly localized plasmonic hotspot. This hotspot exhibits a classic dipolar mode shape, with two strong lobes of enhancement at the particle's equator and a concentrated region directly beneath it. This is the definitive signature of an excited localized surface plasmon resonance (LSPR) coupling its intense near-field energy into the adjacent perovskite,
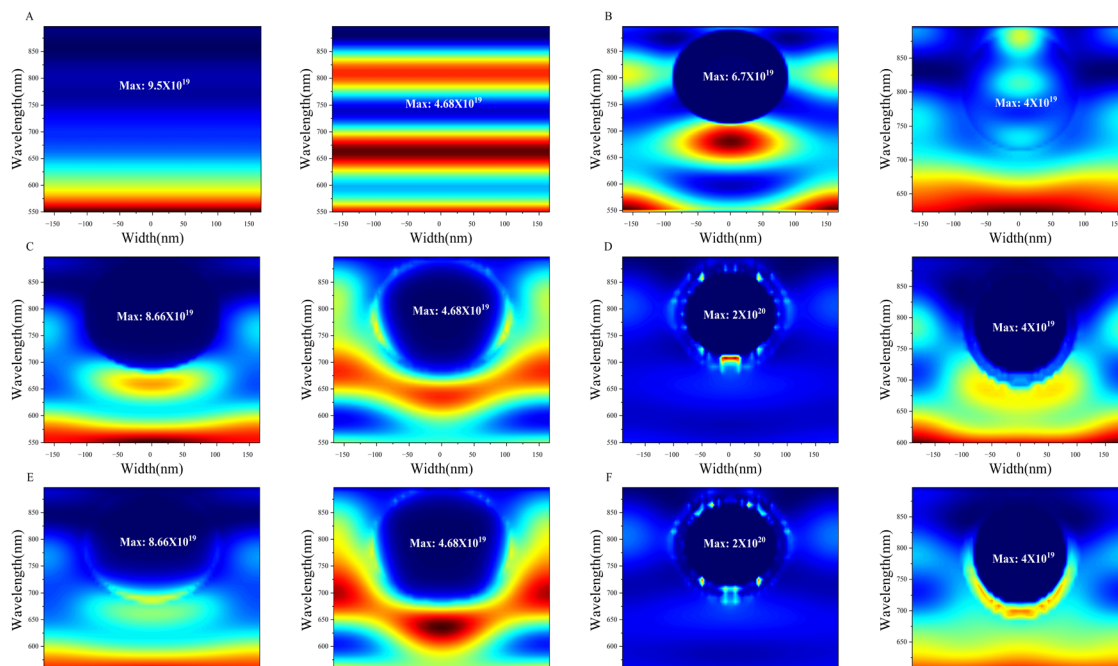
This journal is © The Royal Society of Chemistry 2026

J. Mater. Chem. A, 2026, **14**, 14637–14649 | **14643**

Fig. 7 Spatial profiles of the spectrally-resolved optical generation rate in the perovskite active layer. The architectures shown are: (A) bare planar cell, showing a weak 1D standing wave pattern. (B) dielectric PCGaInP, showing a detrimental "shadowing" effect. (C) Bare plasmonic PCAg, showing a classic dipolar LSPR hotspot. (D) Core–shell plasmonic CoreAg, showing a powerful, higher-order multipolar "necklace" resonance. (E) Bare plasmonic PCAu. (F) Core–shell plasmonic CoreAu.

a powerful 3D mechanism that completely overwhelms the weak 1D interference seen in the baseline.[44]

The addition of a dielectric shell fundamentally alters the nature of the plasmonic resonance, elevating the core–shell design from a simple particle to an advanced optical tuning element. This transformation is best understood through the lens of plasmon hybridization. In a simple, bare nanoparticle, incident light primarily excites the strong dipolar LSPR, while higher-order modes (*e.g.*, quadrupolar) often remain "dark" as they cannot be efficiently excited by a plane wave due to symmetry constraints. The dielectric shell breaks this symmetry, causing the primitive plasmon modes of the metallic core to couple and hybridize, creating new resonant modes and providing a pathway for incident light to channel energy into these previously inaccessible, higher-order modes.

The excitation of such multipolar resonances in core–shell structures is a known physical mechanism; for example, early work on Au@SiO$_2$ nanoshells demonstrated that the shell's geometry could be tuned to excite these higher-order modes.[45,46] However, the strategic implication of this effect for solar cell design has been underexplored. Our work's novelty lies in demonstrating that by treating the shell as an active optical tuner within a complete device architecture, these higher-order modes can be leveraged to execute a superior light management strategy. Instead of focusing on NIR enhancement, we use the shell to enable a powerful broadband anti-reflection in the visible spectrum.

This mechanism is visualized with clarity in the CoreAg device (Fig. 7D). While a full eigenmode decomposition is beyond the scope of this study, the visual evidence is

unambiguous: the dielectric shell has transformed the simple dipolar hotspot of the bare PCAg particle into a stunningly intense, higher-order multipolar resonance, manifesting as a necklace-like series of multiple, discrete hotspots. The peak generation rate within these hotspots reaches 2.0×10^{20} m^{-3}s^{-1}, the highest value observed across all designs. This provides overwhelming visual evidence that the shell's primary optical function is to enable the excitation of these powerful, spatially-concentrated resonant modes. The CoreAu device (Fig. 7F) shows a similar, albeit less intense and more diffuse, higher-order mode structure, confirming that the shell's optical tuning capability is a general principle for both Ag and Au cores.

3.6. Synthesis: impact on short-circuit current density

The preceding optical and spatial analyses have established the precise physical mechanisms governing photon management in each architecture. This culminating section synthesizes these findings to explain the final, terminal device characteristics, beginning with the J_{sc}, which is the most direct consequence of superior optical design.

The total optically-limited J_{sc} is determined by the convolution of the device's EQE with the standard AM1.5 G solar photon flux.[47] Fig. 8 plots both the EQE and the integrated J_{sc} as a function of wavelength, which serves as the bridge between spectral performance and final current output, visually demonstrating how the distinct enhancement strategies translate into tangible performance gains.

The Bare cell, establishes the baseline performance. Its integrated J_{sc} curve rises steadily through the visible spectrum but begins to saturate and flatten significantly beyond 650 nm.

14644 | *J. Mater. Chem. A*, 2026, **14**, 14637–14649

This journal is © The Royal Society of Chemistry 2026

This flattening is the direct consequence of its low EQE in the NIR, confirming its inability to harvest weakly absorbed photons and resulting in a modest final optically-limited current of 18.2 mA cm^{-2}. The dielectric PCGaInP and CoreGaInP devices track the Bare cell's performance closely, with their integrated J_{sc} curves further suppressed by their resonant EQE collapse near 690 nm.

The plot illustrates the competition between the two successful plasmonic strategies. The CoreAu device, leveraging its superior visible-spectrum anti-reflection, takes the lead. By 650 nm, it has already accumulated a significantly higher J_{sc} than all other configurations. Conversely, the NIR-specialist devices, PCAg, PCAu, and CoreAg, initially lag behind. However, their defining feature is the steep, persistent rise of their integrated J_{sc} curves in the 650 nm to 850 nm range, long after the Bare cell's curve has plateaued. This sustained accumulation of current, clearly visible as they begin to catch up to and even surpass some of the other designs, is the direct electrical advantage of their powerful NIR light-trapping resonances.

The final integrated values reveal the winning strategy. While the NIR-specialists make a powerful late surge, they cannot overcome the substantial lead built by the CoreAu device in the photon-rich visible spectrum. The final optically-limited J_{sc} values confirm a clear hierarchy: CoreAu achieves the highest photocurrent potential (26.3 mA cm^{-2}), followed closely by CoreAg (26.1 mA cm^{-2}), with PCAg and PCAu forming a strong second tier. This demonstrates that for this thin-film perovskite system, a holistically optimized strategy that excels at both visible light incoupling and effective NIR light trapping, a feat best accomplished by the CoreAu architecture, yields the greatest overall current enhancement.

3.7. Final device performance: *J–V* characteristics and power conversion efficiency

The final current density–voltage (*J–V*) characteristic encapsulates the interplay of all photogeneration and loss mechanisms

Fig. 8 EQE and integrated short-circuit current density.

into a measurable output.[18] Fig. S4 compares the optically-limited photocurrent potential with the final self-consistent J_{sc} extracted from the full electrical device simulation. This analysis bridges the ideal optical domain with the realities of semiconductor device physics.[48,49] While the CoreAu and CoreAg configurations boast the highest optical potential, they also exhibit the largest absolute recombination losses (~3.3–3.5 mA cm^{-2}). This is not an indication of inferior material quality, but rather an expected consequence of operating at a significantly higher internal charge carrier density (n). Since dominant recombination mechanisms (*e.g.*, radiative, Auger) scale with n^2 and n^3, a higher generation rate inevitably leads to a higher absolute rate of recombination.[50,51] The fact that these devices still deliver the highest final J_{sc} of 26.34 and 26.08 mA cm^{-2} for CoreAu and CoreAg, respectively, confirms that the optical gains are robust enough to far outweigh this inherent increase in recombination.

The *J–V* and corresponding power density–voltage (*P–V*) curves for all seven architectures are presented in Fig. 9a, with the final performance metrics summarized in Table 1. The *J–V* curves clearly illustrate the performance hierarchy established in the optical analysis, segregating the devices into three distinct tiers based on their J_{sc}. The lowest tier consists of the Bare and dielectric devices (18.2–18.8 mA cm^{-2}), the middle tier comprises the bare plasmonic devices (~25 mA cm^{-2}), and the top tier is exclusively occupied by the core–shell plasmonic architectures, which deliver the highest current densities (>26 mA cm^{-2}).

While the differences in J_{sc} are profound, the open-circuit voltage (V_{oc}) and fill factor (FF) are remarkably consistent. The FF is exceptionally high (>85.9%) for all high-performing devices, indicating well-controlled parasitic resistances and efficient charge extraction.[52] A closer look at the V_{oc} reveals a small but systematic decrease of ~10 mV for the core–shell devices (0.954 V) compared to the bare plasmonic devices (0.965 V). A detailed-balance voltage loss analysis, presented in Fig. S5 of the SI, provides the physical explanation for this. The analysis confirms that the non-radiative recombination loss component ($\Delta V3$) is constant, and the minor V_{oc} deficit is instead a predictable optical trade-off.[53,54] It arises from a slight increase in the radiative recombination loss ($\Delta V2$), which is directly tied to the complex resonant spectra of the core–shell designs.[55] This is a critical finding, as it confirms that the performance differences are overwhelmingly dictated by optics, not by any degradation of the device's electronic quality.

The *P–V* curves, which represent the final power output, mirror the hierarchy observed in the *J–V* characteristics. The substantial gains in current translate directly into a superior power-generating capability for the core–shell devices. The final PCE values confirm the unequivocal champion architectures: CoreAu achieves a final efficiency of 21.61%, closely followed by CoreAg at 21.39%. This represents a remarkable 43% relative enhancement over the 15.11% baseline, establishing the optically-tuned core–shell plasmonic design as the superior strategy for enhancing thin-film perovskite solar cells.

Furthermore, a comparison of the final PCE against the Spectroscopically Limited Maximum Efficiency (SLME), shown
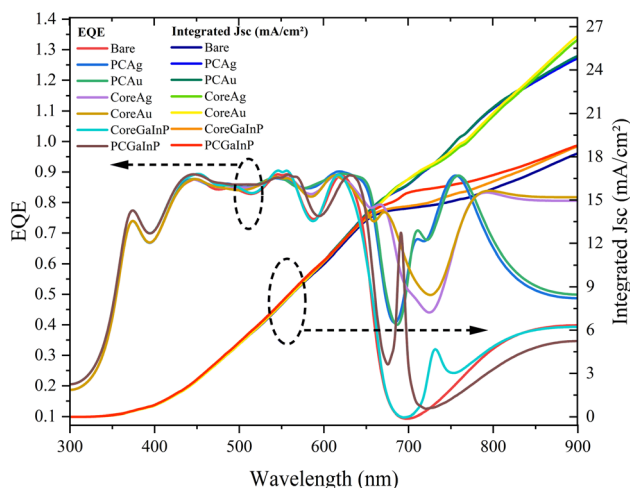
This journal is © The Royal Society of Chemistry 2026

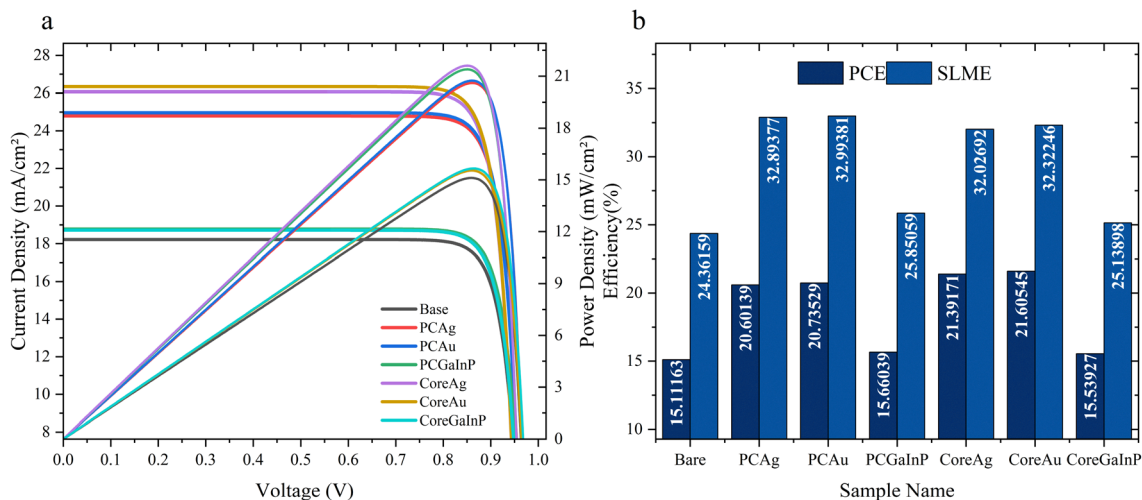*J. Mater. Chem. A*, 2026, **14**, 14637–14649 | **14645**

Fig. 9 (a) J–V and P–V characteristics and (b) PCE and SLME.

Table 1 Key Performance Metrics

Sample name	J_{sc} (mA cm^{-2})	V_{oc} (V)	FF (%)	PCE (%)	SLME (%)
Bare	18.22	0.963	86.09	15.112	24.362
PCAg	24.787	0.965	86.11	20.601	32.894
PCAu	24.963	0.965	86.105	20.735	32.994
CoreAg	26.075	0.954	85.989	21.392	32.027
CoreAu	26.339	0.954	85.987	21.605	32.322
CoreGaInP	18.715	0.964	86.101	15.539	25.139
PCGaInP	18.78	0.968	86.141	15.66	25.851

in Fig. 9b and Table 1, reveals the deeper impact of this optical enhancement. The SLME represents the thermodynamic efficiency ceiling for a given EQE spectrum, assuming perfect, purely radiative electronics.[56,57] The analysis shows that the nanophotonic structures do not merely increase the actual PCE; they fundamentally raise the maximum achievable PCE. The Bare cell, with its poor optical properties, has a relatively low SLME of 24.4%, whereas the champion CoreAu device, by virtue of its superior EQE, raises this thermodynamic ceiling to 32.3%. This demonstrates that the optimized core–shell architecture creates a device that is not just better, but one that is capable of achieving a much higher ideal efficiency, providing a significantly greater headroom for future improvements in material quality.

A final power loss waterfall analysis provides a top-level account of each device's energy budget (see Fig. S6 in the SI).[58] It reveals that the baseline device is fundamentally impaired by a massive Optical Loss of 28.2%, which is its single largest barrier to performance. The success of the champion CoreAu architecture is driven by the drastic reduction of this dominant loss channel to just 12.0%. This superior photon management fundamentally alters the device's energy budget, and as a consequence, Recombination Loss becomes the new primary bottleneck. This provides a clear roadmap for future research: with the optical design now highly optimized, the next major innovation must come from improving material and interface quality to mitigate non-radiative recombination.

4. Limitations and future work

While this computational study provides a robust framework and a clear design principle, its conclusions are based on an idealized model designed to isolate optical phenomena. The primary limitation of this work is its purely optical focus. We have intentionally held the non-radiative recombination parameters constant across all architectures to create a controlled platform for comparing their theoretical optical potential. This is a critical idealization, as the well-documented electronic losses associated with placing bare plasmonic nanoparticles in direct contact with a semiconductor are a known experimental reality that our model intentionally excludes. Our approach allows us to deconstruct the optical trade-offs of the core–shell design with high clarity. A key conclusion from our work is that even if the electronic issues of bare nanoparticles could be perfectly solved, the optically-tuned core–shell architecture still represents a superior strategy due to its ability to excite more effective resonant modes.

The most critical next step is the experimental fabrication and validation of the champion CoreAu architecture. Advanced colloidal synthesis and nano-imprinting techniques will be essential to realize these structures and confirm the predicted performance gains in physical devices. Future modeling efforts should advance beyond the idealizations of this work. A more sophisticated, fully-coupled opto-electronic-thermal framework would allow for the investigation of how intense plasmonic near-fields and localized ohmic heating might affect carrier dynamics and material stability over time. Furthermore, the insights gained here should motivate a broader exploration of the nanophotonic design space. Investigating alternative nanoparticle geometries, different dielectric shell materials, and integration at the front interface could unlock further performance enhancements.

The experimental fabrication of the champion CoreAu architecture, while challenging, is highly feasible with modern techniques. The synthesis of monodisperse ~100 nm gold

nanoparticle cores is a mature process achievable through well-established seeded-growth methods.[59,60] The subsequent deposition of a uniform, conformal $\sim$17 nm dielectric shell such as TiO_2 can be achieved with angstrom-level precision using methods such as Atomic Layer Deposition (ALD). ALD is particularly well-suited for this application as it ensures a complete, pinhole-free coating, which is critical for preventing the electronic quenching that our model idealistically excludes.[61] Alternatively, wet-chemical routes like the Stöber method have also proven highly effective for depositing uniform silica shells on gold cores.[62] While our simulations assume a perfect geometry, the broad spectral nature of the visible enhancement suggests a degree of robustness to minor fabrication imperfections. Based on established plasmon hybridization theory, slight variations in shell thickness or core centering, such as $\pm$1–2 nm, are expected to cause minor, predictable shifts in the resonant peak positions but are unlikely to fundamentally alter the beneficial mechanism of higher-order mode excitation.

Furthermore, this study does not include a thermal analysis of photothermal effects. The parasitic absorption inherent in plasmonic nanoparticles (Fig. 3b) will inevitably be converted into localized heat at the nanoparticle–perovskite interface.[3] This localized temperature increase could have significant implications for real-world device performance and long-term stability. Given the known thermal sensitivity of metal-halide perovskite materials, uncontrolled plasmon-induced heating could potentially act as a local degradation accelerator, compromising the very stability that thin-film designs seek to achieve.[63] While some studies have speculated on potential benefits of localized heating, the risk of accelerated degradation remains the primary concern.[64] A comprehensive investigation of these effects would require a fully-coupled opto-electro-thermal simulation framework, which is beyond the scope of this work. Such models, which correlate nanoscale heat generation with material degradation pathways and temperature-dependent carrier dynamics, represent a critical and necessary next step in designing truly robust and efficient plasmonically-enhanced solar cells.

The most critical overall next step is the experimental fabrication and validation of the champion CoreAu architecture to confirm the predicted performance gains. The insights gained here should also motivate a broader exploration of the nanophotonic design space, investigating alternative nanoparticle geometries, different dielectric shell materials, and integration at the front interface to unlock further performance enhancements.

5. Conclusion

The central challenge in advancing perovskite solar cell technology lies in resolving the inherent trade-off between the efficiency of thick absorbers and the stability of thinner films, a dilemma that necessitates advanced light management. Through a systematic and comprehensive computational analysis, this study has rigorously compared planar, dielectric, bare plasmonic, and core–shell plasmonic architectures within an identical, high-performance PSC platform. We have demonstrated that the core–shell plasmonic nanostructure is the unequivocally superior strategy. The champion CoreAu design achieved a power conversion efficiency of 21.61%, a remarkable 43% relative enhancement over the 15.11% planar baseline, driven by a massive increase in short-circuit current density from 18.22 mA cm^{-2} to 26.34 mA cm^{-2}.

The core physical insight of this work is that the dielectric shell functions as an active resonant tuner, fundamentally altering the nature of the plasmonic response. It is not an optically passive component, but rather an essential tool that enables the excitation of powerful and complex higher-order resonant modes that are inaccessible to simple bare nanoparticles. This mechanism facilitates a critical strategic shift in light management. Instead of narrowly enhancing absorption in the near-infrared where the perovskite is weak, the optimized CoreAu architecture leverages these unique modes to achieve superior broadband anti-reflection in the visible spectrum, maximizing photon capture where the solar flux is greatest.

This study establishes a clear and robust design principle for the next generation of high-efficiency, thin-film photovoltaics. By demonstrating the multifaceted optical superiority of the core–shell paradigm, this work moves the field beyond the simple plasmonics-versus-dielectrics debate and provides a validated, high-performance pathway for overcoming the fundamental absorption-stability dilemma. The findings identify a clear roadmap for progress: having optimized the optical design to a near-ideal state, the primary remaining bottleneck is non-radiative recombination. Future efforts must therefore focus on improving the material and interface quality to fully realize the near-30% efficiency potential of these optically-enhanced architectures.

Conflicts of interest

The authors declare no conflict of interest.

Data availability

All data that support the findings of this study are included within the article.

Supplementary information is available. See DOI: https://doi.org/10.1039/d5ta08034g.

Acknowledgements

References

1 M. A. Green, Solar cell efficiency tables (Version 60), *Prog. Photovoltaics Res. Appl.*, 2022, **30**(7), 687–701.

This journal is © The Royal Society of Chemistry 2026

J. Mater. Chem. A, 2026, **14**, 14637–14649 | **14647**

2 M. M. Lee, J. Teuscher, T. Miyasaka, T. N. Murakami and H. J. Snaith, Efficient Hybrid Solar Cells Based on Meso-Superstructured Organometal Halide Perovskites, *Science*, 2012, **338**(6107), 643–647.

3 T. Leijtens, K. Bush, R. Cheacharoen, R. Beal, A. Bowring and M. D. McGehee, Towards enabling stable lead halide perovskite solar cells; interplay between structural, environmental, and thermal stability, *J. Mater. Chem. A*, 2017, **5**(23), 11483–11500.

4 T. Seyisi, Major challenges for commercialization of perovskite solar cells: A critical review, *Energy Rep.*, 2025, **13**, 1400–1415.

5 S. Khatoon, Perovskite solar cell's efficiency, stability and scalability: A review, *Mater. Sci. Energy Technol.*, 2023, **6**, 437–459.

6 J. Nelson, *The Physics of Solar Cells*, 2003.

7 H. A. Atwater and A. Polman, Plasmonics for improved photovoltaic devices, *Nat. Mater.*, 2010, **9**(3), 205–213.

8 S. Mokkapati and K. R. Catchpole, Nanophotonic light trapping in solar cells, *J. Appl. Phys.*, 2012, **112**(10), DOI: 10.1063/1.4747795.

9 A. I. Kuznetsov, A. E. Miroshnichenko, M. L. Brongersma, Y. S. Kivshar and B. Luk'yanchuk, Optically resonant dielectric nanostructures, *Science*, 2016, **354**(6314), 2472.

10 P. S. Chandrasekhar, *et al.*, Higher efficiency perovskite solar cells using₂ core–shell nanoparticles, *Sustainable Energy Fuels*, 2018, **2**(10), 2260–2267, DOI: 10.1039/C7SE00472A.

11 F. Qi, *et al.*, Improving the performance through SPR effect by employing Au@SiO2 core-shell nanoparticles incorporated TiO2 scaffold in efficient hole transport material free perovskite solar cells, *Electrochim. Acta*, 2018, **282**, 10–15, DOI: 10.1016/j.electacta.2018.06.015.

12 W. Deng, *et al.*, Plasmonic enhancement for high-efficiency planar heterojunction perovskite solar cells, *J. Power Sources*, 2019, **432**, 112–118, DOI: 10.1016/j.jpowsour.2019.05.067.

13 B. Chen, *et al.*, Surface plasmon enhancement of polymer solar cells by penetrating Au/SiO2 core/shell nanoparticles into all organic layers, *Nano Energy*, 2013, **2**(5), 906–915, DOI: 10.1016/j.nanoen.2013.03.011.

14 D.-W. Zhao, *et al.*, Enhanced Efficiency and Stability of Planar Perovskite Solar Cells Using a Dual Electron Transport Layer of Gold Nanoparticles Embedded in Anatase TiO₂ Films, *ACS Appl. Energy Mater.*, 2020, **3**(10), 9568–9575, DOI: 10.1021/acsaem.0c00276.

15 A. Taflove and S. C. Hagness, *Computational Electrodynamics*, Artech House Antennas and Prop, 2005.

16 M. Mahmood, Advancing perovskite solar cells: Unveiling the superior efficiency of copper-doped Strontium Titanate as a novel ETL, *Sol. Energy*, 2024, **279**, 112806.

17 A. A. Tabrizi, H. Saghaei, M. A. Mehranpour and M. Jahangiri, Enhancement of Absorption and Effectiveness of a Perovskite Thin-Film Solar Cell Embedded with Gold Nanospheres, *Plasmonics*, 2021, **16**(3), 747–760.

18 S. Sarkar, Hybridized Guided-Mode Resonances *via* Colloidal Plasmonic Self-Assembled Grating, *ACS Appl. Mater. Interfaces*, 2019, **11**(14), 13752–13760.

19 P. Löper, Complex Refractive Index Spectra of CH3NH3PbI3 Perovskite Thin Films Determined by Spectroscopic Ellipsometry and Spectrophotometry, *J. Phys. Chem. Lett.*, 2014, **6**(1), 66–71.

20 E. D. Palik, in *Handbook of Optical Constants of Solids*, Academic Press, San Diego, 3rd edn, 1998.

21 M. Jelita and H. Saleh, Improvement of Solar Cell Efficiency and Electrical Energy of a Photovoltaic-Thermal System by Using Nanofluid, *J. Kej.*, 2023, **35**(3), 735–745.

22 M. Mahmood, *Superiority of Strontium-Doped Barium Titanate as an Electron Transport for Perovskite Solar Cells for Enhanced Efficiency and Thermal Stability*, Transactions of Tianjin University, Feb, 2025.

23 M. Mahmood, Metal-Doped perovskite oxide Ba(1-x)Sr(x) TiO3 as electron transport layer for enhanced photovoltaic performance: An FDTD study, *Sol. Energy*, 2024, **283**, 112987.

24 S. M. Sze and K. K. Ng, *Physics of Semiconductor Devices*, John Wiley & Sons, Inc, Hoboken, NJ, USA, 2006. DOI: 10.1002/0470068329.

25 A. S. M. Mosabbir, Optimizing Lead-Free Cs2AgBiBr6 Double Perovskite Solar Cells: A Comprehensive Study Using Realistic Simulation Approach, *Sustainable Energy Fuels*, 2024, **8**(18), 4311–4323.

26 E. Hecht, *Optics*, Pearson Education, Inc, Boston, 2017.

27 A. E. Miroshnichenko, S. Flach and Y. S. Kivshar, Fano resonances in nanoscale structures, *Rev. Mod. Phys.*, 2010, **82**(3), 2257–2298.

28 P. R. Bibhu Prasad Nanda, P. Paul, N. Aman, G. S. S and R. Bhatia, Recent Trends and Impact of Localized Surface Plasmon Resonance (LSPR) and Surface-Enhanced Raman Spectroscopy (SERS) in Modern Analysis, *J. Pharm. Anal.*, 2024, **14**(11), DOI: 10.1016/j.jpha.2024.02.013.

29 L. Qiao, Localized surface plasmon resonance enhanced organic solar cell with gold nanospheres, *Appl. Energy*, 2010, **88**(3), 848–852.

30 K. R. Catchpole and A. Polman, Design principles for particle plasmon enhanced solar cells, *Appl. Phys. Lett.*, 2008, **93**(19), 191113.

31 S. Wolf, Organometallic Halide Perovskites: Sharp Optical Absorption Edge and Its Relation to Photovoltaic Performance, *J. Phys. Chem. Lett.*, 2014, **5**(6), 1035–1039.

32 V. E. Ferry, A. Polman and H. A. Atwater, Modeling Light Trapping in Nanostructured Solar Cells, *ACS Nano*, 2011, **5**(12), 10055–10064.

33 K. Zhou, The tradeoff between plasmonic enhancement and optical loss in silicon nanowire solar cells integrated in a metal back reflector, *Opt. Express*, 2012, **20**(S5), 777.

34 A. Bărar, S. A. Maclean, O. Dănilă and A. D. Taylor, Towards High-Efficiency Photon Trapping in Thin-Film Perovskite Solar Cells Using Etched Fractal Metadevices, *Materials*, 2023, **16**(11), 3934.

35 E. Yablonovitch, Statistical ray optics, *J. Opt. Soc. Am.*, 1982, **72**(7), 899.

14648 | *J. Mater. Chem. A*, 2026, **14**, 14637–14649

This journal is © The Royal Society of Chemistry 2026

36 M. A. Green, *Solar Cells : Operating Principles, Technology and System Applications*, Nsw Univ. Of New South Wales, Kensington, 1998.

37 U. Rau, Reciprocity relation between photovoltaic quantum efficiency and electroluminescent emission of solar cells, *Phys. Rev. B:Condens. Matter Mater. Phys.*, 2007, **76**(8), DOI: 10.1103/PhysRevB.76.085303.

38 F. J. Beck, A. Polman and K. R. Catchpole, Tunable light trapping for solar cells using localized surface plasmons, *J. Appl. Phys.*, 2009, **105**, DOI: 10.1063/1.3140609.

39 M. Gantumur, M. Shahiduzzaman, M. H. Ismail, M. Akhtaruzzaman, M. Nakano, M. Karakawa, J. M. Nunzi and T. Taima, Revolutionizing light capture: a comprehensive review of back-contact perovskite solar cell architectures, *Mater. Today*, 2025, **90**, 441–465.

40 R. A. Pala, J. White, E. Barnard, J. Liu and M. L. Brongersma, Design of Plasmonic Thin-Film Solar Cells with Broadband Absorption Enhancements, *Adv. Mater.*, 2009, **21**(34), 3504–3509.

41 R. Hui and M. G. O'Sullivan, "*Characterization of Optical Devices*." pp. 259–363, 2009.

42 A. Vagov, I. A. Larkin, M. D. Croitoru and V. M. Axt, Superanomalous skin-effect and enhanced absorption of light scattered on conductive media, *Sci. Rep.*, 2023, **13**(1), 5103.

43 M. Born, *Principles of Optics*, 1999.

44 L. Novotny and B. Hecht, *Principles of Nano-Optics*, 2009.

45 S. J. Oldenburg, R. D. Averitt, S. L. Westcott and N. J. Halas, Nanoengineering of optical resonances, *Chem. Phys. Lett.*, 1998, **288**(2–4), 243–247, DOI: 10.1016/S0009-2614(98)00277-2.

46 E. Prodan, C. Radloff, N. J. Halas and P. Nordlander, A Hybridization Model for the Plasmon Response of Complex Nanostructures, *Science*, 2003, **302**(5644), 419–422.

47 P. Würfel, U. Würfel, and J. Wiley, *Physics of Solar Cells : from Basic Principles to Advanced Concepts*, Wiley-Vch Verlag Gmbh & Co. Kgaa, Weinheim, 2016.

48 Electrical and Electronic Engineering Programme, *et al.*, Investigation of GeSe Photovoltaic Device Performance *via* 1-Dimensional Computational Modelling, *J. Kej.*, 2024, **36**(3), 1005–1020, DOI: 10.17576/jkukm-2024-36(3)-15.

49 University Moulay Ismail, Morocco, *et al.*, P-type Cu2ZnSnS4 as Multifunctional Material for Photovoltaic and Thermoelectric Application: Theoretical Investigation, *J. Kej.*, 2018, **SI1**(3), 15–22, DOI: 10.17576/jkukm-2018-si1(3)-03.

50 T. S. Sherkar, Recombination in Perovskite Solar Cells: Significance of Grain Boundaries, Interface Traps, and Defect Ions, *ACS Energy Lett.*, 2017, **2**(5), 1214–1222.

51 M. Sayed, On the Investigation of Interface Defects of Solar Cells: Lead-Based *vs.* Lead-Free Perovskite, *IEEE Access*, 2021, **9**, 130221–130232.

52 J. Bisquert, *The Physics of Solar Cells : Perovskites, Organics, and Photovoltaic Fundamentals*, CRC Press, Milton, UNITED KINGDOM, 2017.

53 E. Gutierrez-Partida, Toward Understanding the Built-in Field in Perovskite Solar Cells through Layer-by-Layer Surface Photovoltage Measurements, *ACS Appl. Mater. Interfaces*, 2025, **17**(7), 11176–11186.

54 A. Bothwell, Nonradiative Recombination Dominates Voltage Losses in Cu(In,Ga)Se2 Solar Cells Fabricated using Different Methods, *Sol. RRL*, 2023, **7**(11), 2300075.

55 U. Rau and J. H. Werner, Radiative efficiency limits of solar cells with lateral band-gap fluctuations, *Appl. Phys. Lett.*, 2004, **84**(19), 3735–3737.

56 M. A. Green and A. W. Y. Ho-Baillie, Pushing to the Limit: Radiative Efficiencies of Recent Mainstream and Emerging Solar Cells, *ACS Energy Lett.*, 2019, **4**(7), 1639–1644.

57 T. Kirchartz, J. A. Marquez, M. Stolterfoht and T. Unold, Photoluminescence-Based Characterization of Halide Perovskites for Photovoltaics, *Adv. Energy Mater.*, 2020, **10**(26), 1904134.

58 U. Rau, B. Blank, T. C. M. Müller and T. Kirchartz, Efficiency Potential of Photovoltaic Materials and Devices Unveiled by Detailed-Balance Analysis, *Phys. Rev. Appl.*, 2017, **7**(4), 044016.

59 G. Frens, Controlled Nucleation for the Regulation of the Particle Size in Monodisperse Gold Suspensions, *Nat. Phys. Sci.*, 1973, **241**(105), 20–22, DOI: 10.1038/physci241020a0.

60 N. G. Bastús, J. Comenge and V. Puntes, Kinetically Controlled Seeded Growth Synthesis of Citrate-Stabilized Gold Nanoparticles of up to 200 nm: Size Focusing *versus* Ostwald Ripening, *Langmuir*, 2011, **27**(17), 11098–11105, DOI: 10.1021/la201938u.

61 S. M. George, Atomic Layer Deposition: An Overview, *Chem. Rev.*, 2010, **110**(1), 111–131, DOI: 10.1021/cr900056b.

62 L. M. Liz-Marzán, M. Giersig and P. Mulvaney, Synthesis of Nanosized Gold−Silica Core−Shell Particles, *Langmuir*, 1996, **12**(18), 4329–4335, DOI: 10.1021/la9601871.

63 X. Cui, *et al.*, Photothermal Nanomaterials: A Powerful Light-to-Heat Converter, *Chem. Rev.*, 2023, **123**(11), 6891–6952, DOI: 10.1021/acs.chemrev.3c00159.

64 A. O. Govorov, H. Zhang, H. V. Demir and Y. K. Gun'ko, Photogeneration of hot plasmonic electrons with metal nanocrystals: Quantum description and potential applications, *Nano Today*, 2014, **9**(1), 85–101, DOI: 10.1016/j.nantod.2014.02.006.

This journal is © The Royal Society of Chemistry 2026

J. Mater. Chem. A, 2026, **14**, 14637–14649 | **14649**